Bifacial and semitransparent $Sb_2(S,Se)_3$ solar cells for single-junction and tandem photovoltaic applications

Chen Qian, Kaiwen Sun, Jialin Cong, Huiling Cai, Jialiang Huang, Caixia Li, Rui Cao, Ziheng Liu, Martin Green, Bram Hoex*, Tao Chen*, Xiaojing Hao**

C. Qian, Dr. K. Sun, J.Cong, Dr. J. Huang, Dr. C.Li, Dr. Z. Liu, Prof. M. Green, Prof. B. Hoex, Prof. X. Hao

Australian Centre for Advanced Photovoltaics

School of Photovoltaic and Renewable Energy Engineering

University of New South Wales

Sydney, NSW 2052, Australia

E-mail: kaiwen.sun@unsw.edu.au; b.hoex@unsw.edu.au; xj.hao@unsw.edu.au

H.Cai, R.Cao, Prof. T. Chen

Hefei National Laboratory for Physical Sciences at Microscale

CAS Key Laboratory of Materials for Energy Conversion

Department of Materials Science and Engineering

University of Science and Technology of China

Hefei 230026, China

E-mail: tchenmse@ustc.edu.cn

This article has been accepted for publication and undergone full peer review but has not been through the copyediting, typesetting, pagination and proofreading process, which may lead to differences between this version and the Version of Record. Please cite this article as doi: 10.1002/adma.202303936.

WILEY-VCH

Keywords: Antimony chalcogenide, bifacial, semitransparent, tandem solar cells

Abstract

Thin film solar cells, as a complement to silicon solar cells, are expected to play a significant role in the space industry, building integrated photovoltaic (BIPV), indoor applications and tandem solar cells, where bifaciality and semitransparency are highly desired. $Sb_2(S,Se)_3$ has emerged as a promising new photovoltaic (PV) material for its high absorption coefficient, tuneable bandgap, and non-toxic and earth-abundant constituents. However, high-efficiency $Sb_2(S,Se)_3$ solar cells so far exclusively employ gold back contacts or Mo-coated glass substrates, which only allows monofacial architectures, leaving a considerable gap towards large-scale application in aforementioned fields. Here, we report a bifacial and semitransparent $Sb_2(S,Se)_3$ solar cell enabled by a fluorine-doped tin oxide substrate and an indium tin oxide (ITO) back contact, and its extended application in tandem solar cells. The transparent conductive oxides (TCOs) and the ultra-thin inner n-i-p structure provide high transmittance at the long wavelength region. Despite of the unfavourable Schottky junction and increased defect density at MnS/ITO interface, a power conversion efficiency (PCE) of 7.41% with only front illumination is achieved. On the other hand, though the varied carrier kinetic with rear illumination has a negative impact on the PCE, the internal ultrathin fully depleted absorber layer enables it to remain at a satisfying level at 6.36%, contributing to a great bifaciality of 0.86. As a result, our bifacial and semitransparent $Sb_2(S,Se)_3$ solar cells can gain great enhancement in PV performance by exploiting albedo of surroundings and show exceptional capability in absorbing non-normal incident light. Moreover, our device can be integrated into a tandem solar cell with a bottom silicon solar cell owing to its adjustable bandgap. A $Sb_2(S,Se)_3$/Si tandem solar cell with PCE of 11.66% is achieved in our preliminary trial. These exciting findings imply that bifacial and semitransparent $Sb_2(S,Se)_3$ solar cells possess tremendous potential in practical applications based on their unique characteristics.

1. Introduction

Globally, there are immense efforts being made to develop thin film solar cells for their advantages over market-dominant crystal silicon solar cells, including lightweight, flexibility, and potentially low costs. These distinctive qualities enable them to be an important complement in some specialised application scenarios where crystalline silicon solar cells are not competent, such as the space industry, building integrated photovoltaic (BIPV) and functional indoor applications. High-efficiency thin film solar cells have historically been monofacial and opaque due to the use of metal contacts for both a substrate as well as superstrate configuration. Consequently, they cannot meet the requirement of semi-transparency for BIPV windows [1, 2] and top cells in tandem solar cells and the capability of performing well under non-normal and diffuse incident light. Thus, semitransparency and bifaciality are crucial features for thin film solar cells to function as an essential complement to silicon solar cells.

The concept of bifacial solar cells was first proposed and discussed in 1960s as a feasible technique to further raise the energy yield and potentially allow solar cells to surpass their single junction Shockley-Queisser limit[3]. The first bifacial solar cell was produced from monocrystalline silicon material in 1980[4], followed by multicrystalline silicon [5]. This concept was then applied in dye-sensitized[6-8] and thin film solar cells (e.g. CdTe[9-11], $Cu(In,Ga)S(e)_2$) (CIGS)[12], $Cu_2ZnSnS(e)_4$(CZTSSe)[13, 14], GaAs and perovskite[15]) for flexible, low-weight and semitransparent applications. Bifacial thin film solar cells can be realised in two ways: double-sided deposition, which involves symmetrically growing two cells on each side of the substrate[13], and single-sided deposition, which employs semitransparent front and back contacts (usually polymer[16], transparent conductive oxide (TCO)[17] or graphene[18, 19]) that light can reach the absorber layer from both the front and rear sides. The former type of bifacial solar cells consumes double amount of materials, resulting in complicated fabrication procedures and raises concerns about the interaction from the alternate deposition of both-sided cells. Moreover, the performance deterioration and electrical risk could come from the potential voltage mismatch in the equivalent parallel circuit that results from uneven illumination from both sides in practical applications. On the other hand, single-sided bifacial solar cells have the advantages of being cost-effective, easy to

fabricate and safe to operate. The applicability in BIPV, indoor scenarios, and tandem solar cells is particularly feasible because of its semitransparency, which is another advantage over double-sided bifacial solar cells. However, there are still a variety of challenges, including material selection, fabrication process, and device structure design, remaining to be addressed to enhance the performance of single-sided bifacial and semitransparent solar cells (BSSCs) [20].

Considering the special application area of thin film solar cells discussed earlier, the light-harvesting material should be non-toxic (at least RoHS-compliant), earth-abundant and stable. Low-temperature and one-step fabrication process, in the meantime, is also preferred as this will be easier to upscale. Antimony chalcogenide [$Sb_2(S,Se)_3$] is regarded as a promising candidate and it has recently achieved a 10.7% power conversion efficiency (PCE)[21]. This quasi-1-D material exhibits a tunable bandgap ranging from 1.1 eV to 1.7 eV depending on the ratio of sulfur to selenium (S/Se), providing great potential for applications in not only single-junction but also tandem solar cells[22]. The high absorption coefficient (>10^5 cm^{-1}) enables an ultrathin absorber layer, contributing to high transmittance for photons with an energy below the bandgap. These impressive advantages and steadily increasing PCE highlight the potential and feasibility of employing $Sb_2(S,Se)_3$ in BSSCs. Moreover, the fact that $Sb_2(S,Se)_3$ can directly grow on a transparent FTO substrate enables it to be readily suitable for single-sided BSSCs.

In this work, we demonstrate the first application of $Sb_2(S,Se)_3$ in a single-sided bifacial and semitransparent structure by employing ITO as the back contact capping on the MnS hole-transporting layer (HTL). Unlike the spiro-OMeTAD, MnS demonstrates good crystallinity, allowing it to withstand ion bombardment during the subsequent magneton sputtering for ITO deposition. We then investigated and revealed the underlying mechanism behind the operation of a single-junction bifacial solar cell. In this BSSC, the carrier-generation position and carrier transporting-collecting process have been compared when the solar cell is illuminated from the front side (FTO side) and the rear side (ITO side), respectively. The result implies distinct electrons travelling paths before they are collected. The intrinsic electrical properties of $Sb_2(S,Se)_3$ thin film, such as collection efficiency, deep-level defects and carrier mobility, have discrepant impacts on the performance under front and rear illumination, respectively. Nevertheless, the distinctive ultrathin fully depleted absorber layer (~350 nm) fabricated by the hydrothermal method enables carriers transport via drift instead

of diffusing towards HTL/electron transporting layer (ETL), significantly suppressing the bulk recombination and improving the bipolar transport properties and bifaciality[22-24]. Consequently, a PCE of 7.41% and 6.36% was achieved under front and rear illumination, respectively. In comparison, the conventional gold-based monofacial and opaque solar cell (MOSC) achieved a PCE of 9.50% and 0.70% in respective aforementioned conditions. We identified the apparent performance deterioration of BSSCs under front illumination, particularly open circuit voltage (V_{oc}) drop compared with that of MOSCs, is owing to the potential barrier caused by MnS/ITO Schottky junction and proposed possible strategies for alleviating such loss. Furthermore, innovative characterisation techniques for performance enhancement by exploiting albedo and the capability of absorbing light with sequentially increased tilt incident angles are developed. In practical applications, the BSSC demonstrated significantly promoted performance compared to the MOSC when operating in front of a reflective surface by exploiting the albedo. Moreover, BSSCs exhibit excellent capability of absorbing incident light with sequentially increased tilt angles within a 2π period, implying a good adaptability to real-world applications, whereas MOSCs have stricter requirements for incident angles. Additionally, the exceptional transmittance of BSSC at long wavelengths enables its application in a pioneering 4-terminal $Sb_2(S,Se)_3$/Si tandem solar cells, achieving 11.66% PCE. These findings collectively highlight the significant potential of $Sb_2(S,Se)_3$ BSSCs for widespread applications due to their adjustable bandgap, up-scalable deposition methods, semitransparent properties, and ability to effectively absorb non-vertical incident light. Our work lays the foundation for promoting the practical application of $Sb_2(S,Se)_3$ solar cells.

2. Results and discussion

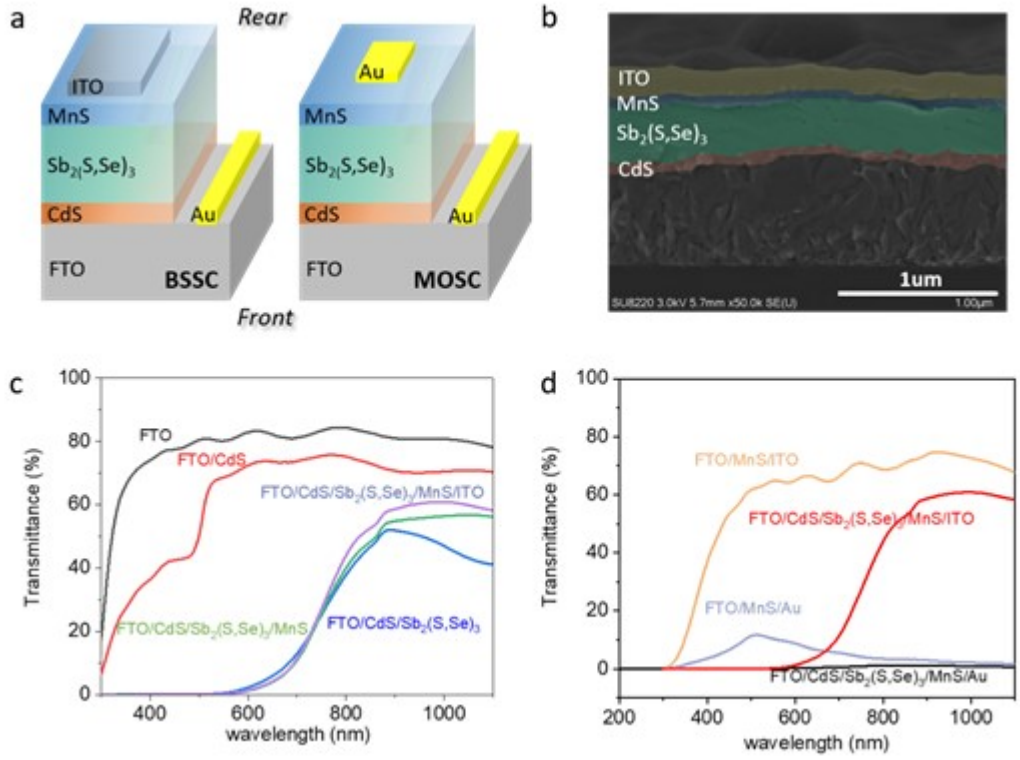

Figure 1. a) The schematic configurations of the $Sb_2(S,Se)_3$ BSSC and MOSC, and **b)** the cross-sectional SEM image of the BSSC. **c)** Transmittance after every sequent deposition step. **d)** Transmittance of the BSSC, MOSC and their corresponding back contacts deposited on FTO-coated glass.

Our BSSCs with a device architecture of FTO/CdS/$Sb_2(S,Se)_3$/MnS/ITO is shown in **Figure 1a**. The chemical bath deposition (CBD) and hydrothermal method were respectively used for the deposition of the CdS electron transporting layer and $Sb_2(S,Se)_3$ absorber layer as described in our previous work[22]. The obtained $Sb_2(S,Se)_3$ absorber layer is often significantly thinner than that deposited using the vapour thermal deposition (VTD) or rapid thermal evaporation (RTP) methods (350nm

versus 1 um), resulting in a fully depleted absorber layer. MnS was employed as the hole transport layer for its competitive performance, excellent stability[22], and most importantly, great tolerance to the subsequent sputtering process compared with spiro-OMeTAD which is commonly used in high-efficiency superstrate-configuration $Sb_2(S,Se)_3$ solar cells as shown in **Table S1**. The ITO layer was then grown on top of MnS, serving as back contact in our BSSC. All the fabrication processes prior to ITO or Au deposition were controlled to be identical for eliminating variates when comparing $Sb_2(S,Se)_3$ BSSCs and MOSCs in our work. Herein, we regard the FTO side as "front" side while the ITO side as "rear" side for distinction and discussion. **Figure 1b** shows the cross-sectional scanning electron microscopy (SEM) image, demonstrating that all layers, particularly MnS and ITO layers, have good coverage and thickness uniformity, which satisfies the technical requirements of large-area and up-scaling manufacturing.

We measured the transmittance of the BSSC after each sequent deposition step to identify the degree of transparency and potential parasitic optical losses. **Figure 1c** points out that the coated MnS and ITO layers do not lower the transmittance due to their higher bandgaps than $Sb_2(S,Se)_3$, but result in an increased transmittance from a wavelength of 900 nm instead. The phenomenon can be explained from two perspectives: the suppression of optical reflectance at back surface and the removal of low bandgap oxidized top surface. The MnS or MnS/ITO serves as an anti-reflection coating (ARC) to prevent the cave effect in transmittance, as illustrated in detail in **Figure S1**. Moreover, the dispersion of aggregated oxygen on top surface of $Sb_2(S,Se)_3$, as revealed by ref. [22], as well as the unintentional etching of the oxidized surface layer of MnS during the subsequent sputtering process, as evidenced by energy dispersive spectrometry (EDS) in the following section, also contributes to the respective improvement in light transmittance after the sequential deposition of MnS and ITO. Consequently, the transmittance of the BSSC starts to rise rapidly when the wavelength goes beyond the absorption edge of $Sb_2(S,Se)_3$ at around 850nm and finally reaches near 60%. Meanwhile, **Figure 1d** displays that BSSCs exhibit a substantially higher transmittance at the long wavelength region than MOSCs, owing to the excellent transparency of the ITO back contact.

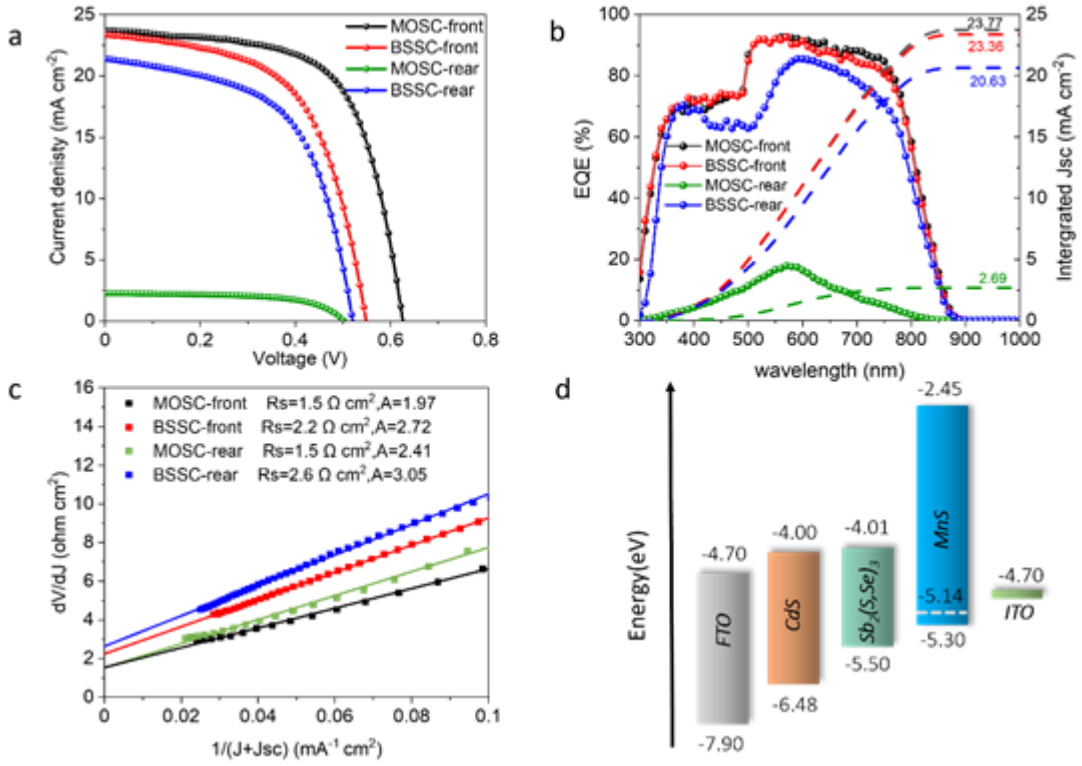

Figure 2. a) J-V curve, **b)** EQE response, and **c)** diode characteristics of $Sb_2(S,Se)_3$ MOSCs and BSSCs with front and rear illumination, respectively (series resistance Rs and diode ideality factor A were obtained according to ref.[25]). **d)** Band diagram of $Sb_2(S,Se)_3$ BSSCs (the dash line refers to Fermi level).

Table 1. PV performance of the $Sb_2(S,Se)_3$ MOSC and BSSC with front and rear illumination by AM1.5G light, respectively.

Device	V_{oc}/V	J_{sc}/mA cm^{-2}	FF/%	PCE/%
MOSC-front	0.623	23.7	64.5	9.50
MOSC-rear	0.504	2.29	61.5	0.70
BSSC-front	0.541	23.4	58.3	7.41
BSSC-rear	0.522	21.4	57.3	6.36

To evaluate the bifaciality, we compare the IV performance (details in **Table 1)** and external quantum efficiency (EQE) response of MOSCs and BSSCs under front and rear illumination, respectively, in **Figure 2a&b**. The PV performance of MOSCs under rear illumination exhibits a dramatic downtrend because Au back contact blocks most of the light. J_{sc} drops from 23.7 mA cm^{-2} under front illumination to only 2.29 mA cm^{-2}. Additionally, the EQE curve of the MOSC-rear is in good agreement with the transmittance of FTO/MnS/Au sample spanning from 300 to 800 nm. The MOSC-rear case thereby exhibits a dramatically worse PV performance and ideality factor (A=2.41) as shown in **Figure 2c**, compared with the MOSC-front case.

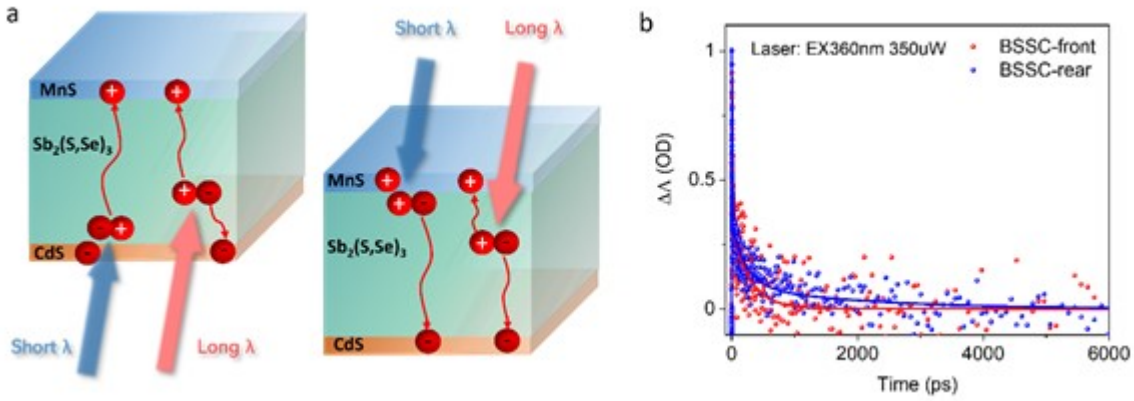

Figure 3. a) The schematic diagram of the carrier generation, transport and collection process under front illumination (left) and rear illumination (right), respectively, and **b)** kinetic study of photo-generated carriers with front and rear illumination, respectively in BSSCs.

Table 2. Coefficient extracted from triexponential fitting the transient absorption spectra data.

	A_1	τ_1/ps	A_2	τ_2/ps	A_3	τ_3/ps
BSSC-rear	68.75%	2.0	22.50%	230	8.75%	2000
BSSC-front	75.33%	1.6	24.48%	280	0.19%	20000

In contrast, the BSSCs exhibit excellent bifaciality of 0.86, showing comparable PV performance under rear illumination. In the EQE curve of BSSC-rear case, the apparent collapse between 420-500 nm after an initial sharp increase, followed by a subsequent increase, is also observed in substrate configuration solar cells (note that our BSSC can be regarded as a substrate configuration in the case of rear illumination), such as kesterite and chalcopyrite solar cells. This behaviour is attributed to light interference and can be eliminated by using a MgF_2 ARC[26]. Furthermore, the source of the parasitic absorption in BSSC-rear is hard to be clearly identified. Mn is an element that can exist in multiple valence states. Therefore, the incorporation of dispersed oxygen originating from the $Sb_2(S,Se)_3$ top surface into MnS may lead to the formation of various oxides, including MnO_2, MnO, Mn_2O_3 and Mn_3O_4. They exhibit a bandgap of 1.6-2.3 eV[27], 2.36 eV[28], 2.0 eV[29], and 2.2 eV[30],

respectively, all of which are lower than the bandgap of MnS. Therefore, the observed parasitic absorption under rear illumination cannot be solely attributed to MnS but also to MnO_x. The presence of MnO_x in bulk MnS influences the shape of the EQE curve and results in the rapid increase in EQE from 500-600 nm. With the investigation on the carriers dynamics, we are aware of the fact that the EQE at the short wavelength region depends on the collection of photo-generated carriers near the $Sb_2(S,Se)_3$/MnS interface, as illustrated in **Figure 3a right.** This part of photo-generated electrons must travel through the entire absorber layer and finally be collected by electron transport layer [31]. The average travelling distance of electrons is increased while that of holes is shortened, compared with those under front illumination in **Figure 3a left**. Thus, the capture and recombination processes vary in the BSSC-rear case because of different collection efficiency of CdS and MnS, two deep level hole traps in $Sb_2(S,Se)_3$ bulk [32], and different mobility of electrons (15 $cm^2 \cdot V^{-1} \cdot s^{-1}$) and holes (42 $cm^2 \cdot V^{-1} \cdot s^{-1}$) in $Sb_2(S,Se)_3$ [33]. These underlying reasons explain why the BSSC-rear is lower than BSSC-front in EQE response and accordingly in PV performance. However, the bifaciality is still satisfying at 0.86, which mainly benefits from the ultrathin fully depleted $Sb_2(S,Se)_3$ absorber layer as previous research uncovered that the thinner absorber layers typically result in a higher bifaciality[11, 24, 34]. We also conducted transient absorption spectrum (TAS) to compare the kinetics of carrier transporting with front and rear illumination. Ultrathin $Sb_2(S,Se)_3$ (30-50nm) films were fabricated to ensure that the excitation and emission signals could be detected clearly with a picosecond resolution. **Figure 3b** shows the transient kinetic traces (decay of photo-induced absorption) of front- and rear-illuminated measurements. The decay of photo-induced absorption (PIA) was fitted using triexponential functions. The results are shown in **Table 2**. The shortest decay time τ_1 could be dominated by the carrier extraction process driven by the built-in electric field, whilst the longest decay time τ_3 could be dominated by the trapping-detrapping and/or non-radiative recombination processes at the ETL/absorber or absorber/HTL interfaces, and τ_2 is dominated by the combined processes[35]. BSSC-rear shows a similar τ_1 as the BSSC-front, agreeing with the largely unaltered built-in electric field. However, when it comes to τ_3, the BSSC-front shows much longer decay than that of the BSSC-rear case, illustrating less interface trapping at CdS/$Sb_2(S,Se)_3$ than $Sb_2(S,Se)_3$/MnS, which may also be responsible for its higher J_{sc} and *FF*.

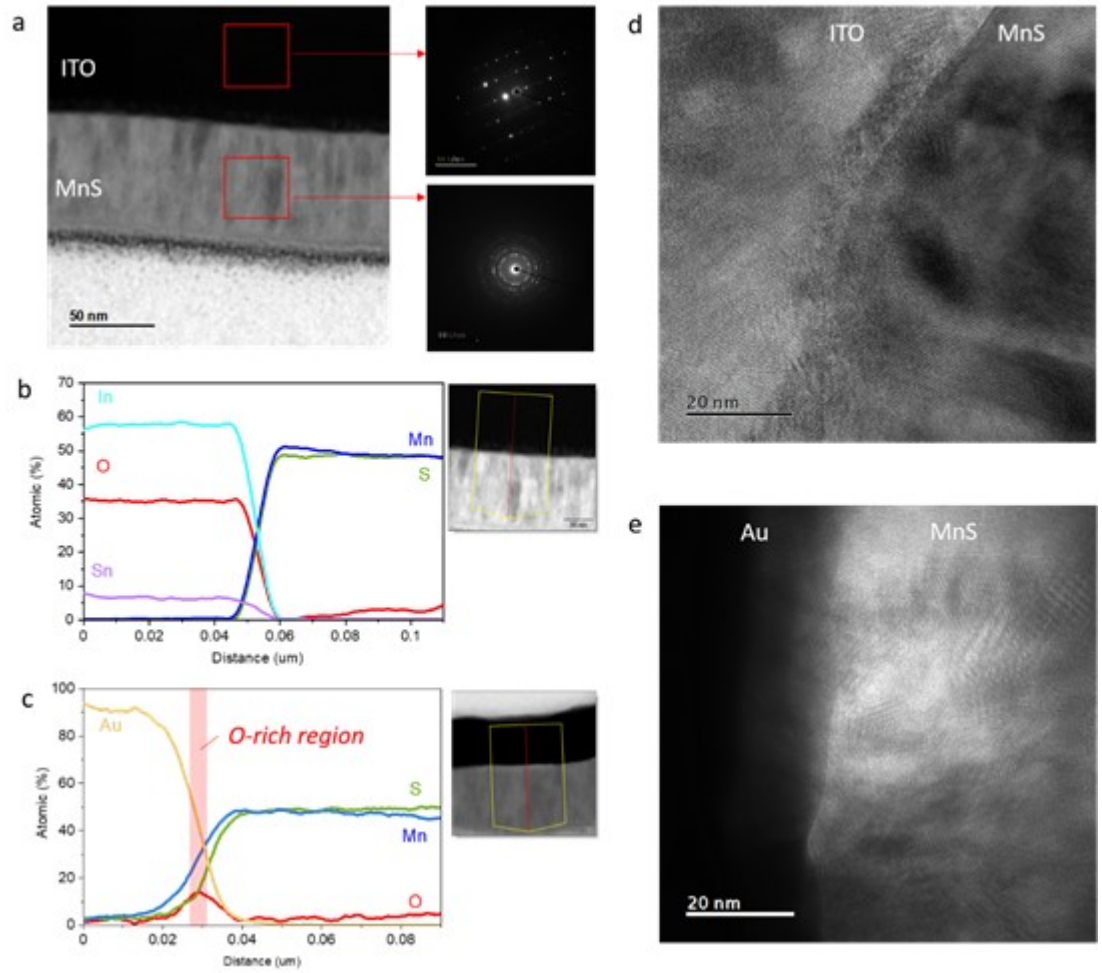

Figure 4. a) Bright field TEM image at MnS/ITO interface and selected area diffraction (SAD) pattern of the MnS and ITO layer. EDS line scan along the depth through **b)** MnS/ITO interface and **c)** MnS/Au interface. Local TEM of **d)** MnS/ITO interface and **e)** MnS/Au interface.

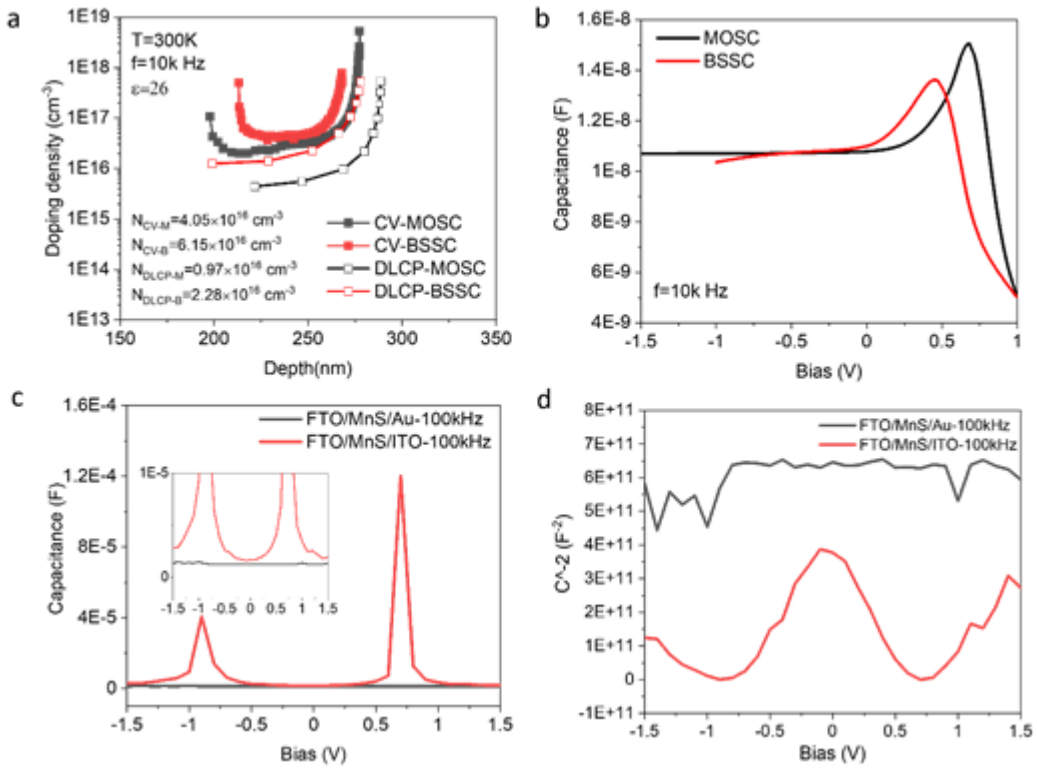

Figure 5. a) defect concentration (Nd)-depth (W), and **b)** C-V of MOSCs and BSSCs, respectively. **c)** C-V and **d)** M-S curves of FTO/MnS/Au and FTO/MnS/ITO samples, respectively. (The capacitance values have been normalised to 0.12 cm^2.)

Though a good bifaciality was obtained in our BSSC, the employment of transparent back contact did cause detrimental effects on the PV performance, particularly V_{oc} (0.541V vs 0.623V) and FF (58.3% vs 64.5%) when comparing with MOSCs under front illumination (**Table 1)**. This might relate to the physical interface quality, such as lattice dislocation and interface defects, or band alignment issues of MnS/ITO. We thereby did an investigation to comprehend the underlying principles of the gap in order to further improve the performance of $Sb_2(S,Se)_3$ BSSCs.

To analyse the interface property microscopically, transmission electron microscopy (TEM) was conducted. The MnS layer shows crystalline structure as revealed in the selected area diffraction (SAD) pattern and high-resolution TEM mage in **Figure 4a**, probably contributing to its good

tolerance to the high-energy bombardment during the subsequent magnetron sputtering process. Interestingly, the EDS line scan in **Figure 4b&c** and mapping in **Figure S2** support the proposal that the ion bombardment seems to etch the ultra-thin oxidized surface layer of MnS with a narrower bandgap than pure MnS, partially explaining the further increased transmittance after depositing ITO layer for wavelengths >900 nm as displayed in **Figure 1c**. As shown in **Figure 4d**, ITO layer is not epitaxially grown on MnS, but a sharp interface can be observed, and additionally, MnS near the interface shows similar crystallinity as in the bulk. Therefore, severe physical sputtering damage to the interface due to ion bombardment can be eliminated in this case.

Another probable cause regarding interface defects was proposed after comparing the EQE response in **Figure 2b**. BSSC-front exhibits a lower EQE value between 600 nm to 800 nm wavelength than MOSC-front, manifesting less efficient carrier extraction at MnS/ITO interface than at the MnS/Au interface. The presence of more interface defects and shunt paths is also indicated by larger diode ideality factor *A* arising from the fitting results in **Figure 2c** (2.72 for BSSC-front and 1.97 for MOSC-front). To further determine the number of interface defects, we implemented deep-level capacitance profiling (DLCP) and capacitance-voltage (C-V) to characterise junction interface defects density through their deviation, as DLCP is less sensitive to junction interface defects than C-V. C-V measurements were performed at a frequency of 10k Hz. **Figure 5a** displays the profile of defect concentrations against depth and the concentration numbers at zero bias evaluated from C-V and DLCP results. We calculated an interface defect areal density of 1.35×10^{12} cm^{-2} in BSSCs, higher than 1.07×10^{12} cm^{-2} in MOSCs, which therefore led to more interface recombination and contribute to lower FF and Voc in BSSC-front case.

The band alignment at the MnS/ITO interface was also explored in response to the severe V_{oc} drop. The ultraviolet photoelectron spectroscopy (UPS) measurement in **Figure S3** located the Fermi level of the ITO thin film at -4.7 eV, which is 0.44 eV higher than that of MnS thin film as shown in **Figure 2d**[22]. The band inevitably bends downwards at the interface since the back contact functions as a hole-extraction layer. This Schottky contact at MnS/ITO interface creates a potential barrier against the built-in potential generated by $CdS/Sb_2(S,Se)_3$/MnS and results in a diminished output potential, explaining why the capacitance of BSSCs starts to collapse at a lower positive bias than that of

MOSCs in **Figure 5b**. As a result, the fitted built-in potential from the Mott-Schottky (M-S) curves were 0.95 eV and 1.15 eV for BSSCs and MOSCs, respectively, as shown in **Figure S4**.

To investigate the Schottky contact specifically, we deposited MnS/ITO and MnS/Au directly on FTO-coated glass and measured the capacitance against voltage, respectively. **Figure 5c** illustrates that FTO/MnS/ITO exhibits a constant capacitance of 10 nF between -0.50 V and 0.35V bias and two sharp signals on the edge of this region. At $V=V_{bi}$, the flat band condition was achieved due to the collapse of the depletion region, thereby diminishing the contribution of depletion capacitance[36]. Therefore, the occurrence of signals demonstrates the existence of depletion region in both MnS and ITO layers near the interface, i.e. a junction and an electric field[37]. The collapse may be attributed to the significant carrier injection at forward as well as backward bias. The asymmetric positions of those two signals result from different carrier concentrations in MnS and ITO and, accordingly, different widths of depletion regions located in the corresponding layer. FTO/MnS/ITO exhibits a positive and a negative slope in two quadrants of *M-S* profile, whereas FTO/MnS/Au shows a horizontal line, as displayed in **Figure 5d.** We then lowered the applied frequency to a minimum of 1k Hz in **Figure S5** to confirm that this phenomenon is not accidentally happening at high frequencies. These characterisation results firmly revealed that the unfavourable upward band bending significantly reduces the charge transport efficiency at the MnS/ITO interface and vitally accounts for *Voc* and FF drop of BSSCs employing ITO back contact compared with MOSCs with Au back contact. Consequently, adjusting the Fermi level of ITO or MnS for well-aligned bands could address the potential barrier and improve the performance of BSSCs.

Table 3. PV performance of the MOSC and BSSC with front illumination by AM1.5G 1-sun light on a standard photovoltaic test platform (no back reflection) and on a "white filter paper (WP)".

Device	Voc/V	Jsc/mA cm^{-2}	FF/%	PCE/%
MOSC-front	0.623	23.7	64.5	9.50
MOSC-front on WP	0.614	24.3	64.4	9.57
BSSC-front	0.541	23.4	58.3	7.41
BSSC-front on WP	0.529	28.2	56.5	8.39

BSSCs possess advantages over MOSCs in absorbing diffuse or reflected light from the environment by exploiting the albedo. The performance of a MOSC shows tiny relation to the albedo of the background while, in contrast, the performance of a BSSC can be improved apparently if the background exhibits a certain albedo instead of absolute black. The transmitted light can be partially reflected, goes through the semitransparent ITO layer, and be re-absorbed by $Sb_2(S,Se)_3$ again. The increase in short circuit current density (J_{sc}) depends on the reflectivity and rear EQE and can be calculated by:

$$Increased\ J_{SC} = \int_{\lambda_1}^{\lambda_2} q \times AM1.5G \times T \times R(bg) \times EQE(rear)\, d\lambda \qquad (1)$$

Where, $\lambda_1$and λ_2 are the absorption spectra edge, q is elementary charge, T is transmittance of BSSCs, R (bg) is reflectivity of background, EQE (rear) is external quantum efficiency when light comes from the rear side. We thereby calculated the increased J_{sc} to be 4.72 and 0.04 mA cm^{-2} for BSSCs and MOSCs, respectively. On the other hand, **Table 3** displays the measured IV parameters of the same devices in **Table 1** on a “white” background which was established using a white filter paper (WP) with a reflectivity of >70% as shown in **Figure S6.** The IV parameters tested on a standard platform are listed together for comparison. The enhancement of J_{sc} was 4.85 and 0.58 mA cm^{-2}, respectively, well consistent with the theoretical calculation. The great enhancement of BSSCs improves PCE by 13.3% relative, compared with only 0.7% in MOSCs.

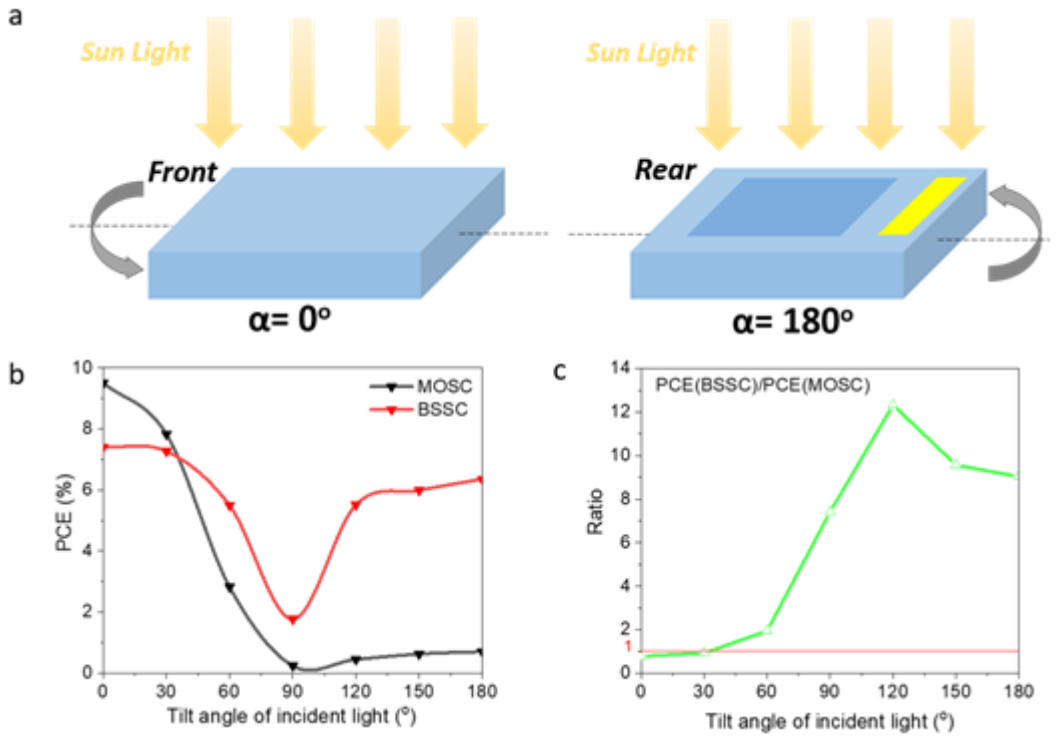

Figure 6. a) Schematic diagram for measuring PV performance against rotation angles. **b)** PCE of MOSCs and BSSCs, and **c)** their corresponding ratios against tilt angles of incident light.

The superiority of BSSCs in practical applications is also reflected in their excellent handling of abnormal incident light. We rotated the devices and measured the PV performance to simulate the actual application scenario with incident light from 0 to 180 degrees. Herein, zero degrees denotes the condition where the front side faces the incident light as shown in **Figure 6a**. **Figure 6b** demonstrates that the output power of the MOSC can become essentially zero once the rotating angle gradually goes beyond 90 degrees, which is mainly attributed to a significantly reduced J_{sc} as seen in **Figure S7**. In contrast, the $Sb_2(S,Se)_3$ BSSC exhibits a quasi-sin wave type behaviour with an expected period of 2π, benefiting from the great bifaciality. The tendency is in line with the earlier study's results, which indicated a sine wave with a period of π for symmetrically growing biolithic bifacial solar cells[13]. **Figure 6c** manifests that our BSSCs can operate better than MOSCs when the

incident light illuminates with a tilt angle larger than 30 degrees. Particularly when the tilt angle exceeds 90 degrees, the advantage can be as much as nine times or greater.

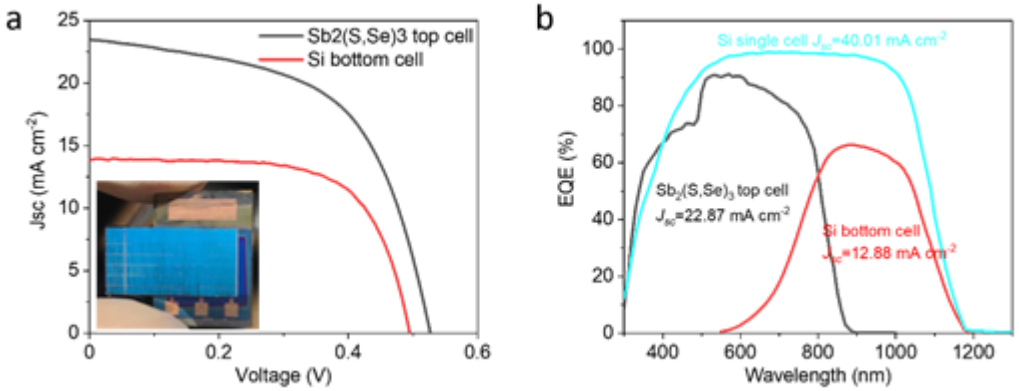

Figure 7. a) J-V curves of the $Sb_2(S,Se)_3$ semitransparent top cell and Si bottom cell. B) EQE curves of the $Sb_2(S,Se)_3$ semitransparent top cell, Si bottom cell covered by the $Sb_2(S,Se)_3$ semitransparent top cell, and Si cell alone.

Table 4. PV parameters of the $Sb_2(S,Se)_3$ semitransparent top cell, Si bottom cell with a $Sb_2(S,Se)_3$ top cell filter and the 4-terminal tandem cell.

Device	V_{oc}/V	J_{sc}/mA cm^{-2}	FF/%	PCE/%
$Sb_2(S,Se)_3$ top cell	0.526	23.5	57.0	7.05
Si bottom cell with a top cell filter	0.492	13.9	67.5	4.61
4-T tandem cell				11.66

Owing to the suitable bandgap and high transmittance at long wavelengths, our BSSCs are applicable as top cells in tandem solar cells to increase the overall efficiency and energy yield. Transmitted light beyond the absorption spectra of $Sb_2(S,Se)_3$ can be efficiently absorbed by a bottom cell with a narrow bandgap, such as a silicon solar cell. We therefore fabricated a 4-terminal (4-T) tandem solar

cell by stacking our BSSC with ITO side facing down on a Si heterojunction (HJT) solar cell. The structure of the tandem solar cell is depicted in **Figure S8**. A polydimethylsiloxane (PDMS) film with random, pyramidal textures was introduced at the top surface of the tandem cell to minimise the reflection loss[38]. IV parameters and EQE responses in **Figure 7** and **Table 4** reveal that Si bottom cell can actually absorb the long-wavelength light transmitted through the $Sb_2(S,Se)_3$ top cell, and then provides additional photoelectric conversion. Therefore, the 4-T $Sb_2(S,Se)_3$/Si tandem solar cell achieved a PCE of 11.66%, breaking the PCE record of emerging single-junction $Sb_2(S,Se)_3$-based solar cells with ease. It implies the significance of developing BSSCs and tandem solar cells. Furthermore, there is a big potential for further optimising this preliminary tandem cell design and fabrication process to achieve higher efficiency. Since the Si bottom cell in this work is cut from a commercial size large cell, employing a matched-size Si cell with an optimised structure and less edge recombination will improve the bottom cell performance. Additionally, the bandgap of $Sb_2(S,Se)_3$ top cell can be adjusted by varying the dose of selenourea to better match the bandgap of the Si subcell, enabling better tandem efficiency.

3. Conclusion

In summary, we demonstrate bifacial and semitransparent $Sb_2(S,Se)_3$ solar cells by employing FTO-coated glass as a substrate and a sputtered ITO layer as back contact. This sandwich structure of TCO/n-i-p architecture/TCO provides a great bifaciality with the aid of an ultrathin fully depleted $Sb_2(S,Se)_3$ absorber layer. As a result, PCE of 7.41% under front illumination and 6.36% under rear illumination are obtained despite the detrimental Schottky contact between MnS and ITO. The discrepancy attributes to reversed kinetics of carrier transport and diverse electron travelling distance in these two cases. Because of the excellent semitransparency and bifaciality, it can effectively gain enhancement by exploiting albedo and well handle the tilt incident light, providing feasibility and superiority for practical applications, such as the space industry, indoor applications, BIPV and tandem solar cells. We subsequently assembled a 4-T tandem solar cell using a Si bottom cell, achieving an overall PCE of 11.66%. All these exciting results show that bifacial and semitransparent $Sb_2(S,Se)_3$ solar cells have exhibited tremendous potential and advantages in large-

scale practical application, owing to RoHS-compliance, low cost, low-temperature fabrication process and exceptional bifaciality.

4. Experimental Section/Methods

Deposition of back contact

Magneton sputtering was used to deposit an ITO layer on top of FTO/CdS/$Sb_2(S,Se)_3$/MnS. The specimens were attached to a round sample holder by double sticky tape and then covered by a customised shadow mask, resulting in a 0.84 cm^2 ITO layer on top of MnS. Followed by that, the sample holder was inserted along the groove to the reserved spot in the sputtering machine (JGP-450A, Sky technology development Co., Ltd. Chinese Academy of Sciences), with MnS side facing down towards the ITO target material (purchased from Beijing Zhongnuoxincai). Self-rotating was turned on to improve the uniformity of ITO thin film. The Ar gas flowed into the chamber once the pressure reached 5×10^{-4} Pa and the rate should be adjusted to stabilise the pressure at 0.7 Pa. Afterwards, ITO was deposited at 40 W (9 W reflected) sputtering power for 15 minutes.

Fabrication of devices

FTO-coated glasses (purchased from Liaoning Youxuan Tech. Co., Ltd.) were pre-cleaned by deionised (DI) water, isopropanol, acetone, and ethanol (Materials without specifically pointed out were all purchased from Sinopharm Chemical Reagent Co., Ltd.) for 40 minutes sequentially. UV ozone cleaner (HF-Kejing, PCE-22-LD) was employed to clean the FTO substrate before use. The cadmium sulfide layer was deposited on FTO substrate by the chemical bath deposition (CBD) method.[32] Then $CdCl_2$ (20mg in 1mL methanol) was spin coated at 3000 rpm for 30 seconds and sample was heated at 400℃for 10 minutes in air to improve the grain size of the CdS layer and incorporate Cl and O into the film. This results in a better surface condition for epitaxial growth of $Sb_2(S,Se)_3$ in an autoclave reaction[39]. After that, $Sb_2(S,Se)_3$ layer was deposited by the hydrothermal method. Specifically, 20 mM antimony potassium tartrate, 80 mM sodium thiosulfate tetrahydrate and 23 mg selenourea (99.97%, Alfa Aesar) were added sequentially into a Teflon autoclave (50 mL nominal

volume) with 40 mL DI water. The substrate inclined to the inside surface at 75°. Then the autoclave was sealed into a stainless-steel tank and heated in an oven (Shanghai Jinghong, JHG-9023A) up to 130℃ for 130 minutes. After natural cooling to room temperature, the samples were taken out, and swilled with DI water and ethanol before being dried for 1 minute in a vacuum dryer (Shanghai Jinghong, DZF-6030) where the temperature was kept at 110℃ and the air pressure was 10 kPa. Afterwards, the samples were transferred to a nitrogen-filled glove box and annealed at 350℃ for 10 minutes for crystallisation. Subsequently, the MnS HTL was grown by thermal evaporation and post-treated as our previous paper[22]. Finally, a gold anode was deposited by thermal evaporation under a pressure of 5×10^{-4} Pa. Eventually, the thicknesses of CdS, $Sb_2(S,Se)_3$, MnS, and ITO layers are 60, 350, 80 and 160 nm, respectively, in a typical device. The Si bottom cell is cut from a commercial size HJT solar cell and epoxy is used as the intermediate layer to achive optical matching.

Characterisation of thin films

The morphology and element ratios of MnS thin films and devices were characterised by SEM (HITACHI UHR FE-SEM SU8200) with an EDS module (Oxford, AZtec X-Max 50), detecting elements from B(5) to U(92). The bandgap was measured by UV-vis (SOLID 3700). The hole extraction capability was measured by transient absorption spectrum (Helios, Ultrafast System LLC), where a nondegenerate pump-probe configuration was applied to probe the transient dynamics (100 fs to 7 ns). Additionally, the pump and probe laser pulses were generated by frequency doubling the fundamental output (Coherent Vitesse, 80 MHz, Ti-sapphire laser) and white light generated with a sapphire plate, respectively. The decay characteristics were fitted by a triexponential model $y = \Sigma A_i \exp(-x/t_i)$.

Characterisation of solar cells

The J–V characteristics were determined using a Keithley 2400 apparatus under an AM 1.5 illumination with an intensity of 100 mW cm^{-2} provided by a standard xenon-lamp-based solar simulator (Oriel Sol 3 A, Japan). Before the test, the illumination intensity of a solar simulator was calibrated by a monocrystalline silicon reference cell (Oriel P/N 91150 V, with KG-5 visible colour filter), previously standardised by the National Renewable Energy

Laboratory (NREL). Both sides of the device were covered by opaque masks with a 0.04 cm^2 aperture respectively. Black opaque tap was used to cover side surfaces of the glass substrate to prevent ambient light from leaking into the device (**Firgure.S10**). The EQE (model SPIEQ200) was measured by a single-source illumination system (halogen lamp) coupled with a monochromator. Transmission electron microscopy TEM (JEOL F200) was used to determine the interface condition. The cross-section TEM samples with thickness around 100nm were prepared by a focused ion beam (FIB) equipped with micro-manipulator for in-situ lift-out (Thermo Fisher Helios G4 PFIB). The C-V characterisation was performed using Keysight E4990A Impedance Analyzer at a frequency of 10k-100k Hz in the dark, ranging from -1.5 V to 1.5 V.

Author contributions

X.H, B.H, M.G and K.S supervised the project at the University of New South Wales, while T.C supervised the project at the University of Science and Technology of China. C.Q conceived the original concept, designed the experiments, fabricated the devices, conducted the photovoltaic and optical characterisation, analysed data and wrote this manuscript. J.C and J.H performed TEM and EDS measurements and analysed the result. J.H conducted C-V and DLCP measurements. R.C conducted TAS characterisation. H.C measured the reflectivity of white filter paper. C.L and Z.L deposited PDMS layer and measured the PV performance of the tandem cell. X.H, B.H, T.C and K.S revised this manuscript with all authors commenting on the manuscript.

Conflicts of interest

There are no conflicts to declare.

Acknowledgements

This research has been financially supported by the Australian Renewable Energy Agency (ARENA) (Grant No. 2020/RND014), National Natural Science Foundation of China (U19A2092 and 22275180), National Key Research and Development Program of China (2019YFA0405600), and Hefei Science Center, Chinese Academy of Sciences (2022HSC-CIP006). The authors acknowledge the facilities and

the scientific and technical assistance of the Electron Microscope Unit (EMU) at the University of New South Wales (UNSW). C.Qian acknowledges University International Postgraduate Award (UIPA) scholarship funded by University of New South Wales. K.S acknowledges the support from Australian Centre of Advanced Photovoltaics (ACAP) as a recipient of ACAP Fellowship (RG172864-B). The views expressed herein are of the authors but not of the Australian Government, ARENA or ARC.

Supporting Information

Supporting Information is available from the Wiley Online Library or from the author.

Received: ((will be filled in by the editorial staff))
Revised: ((will be filled in by the editorial staff))
Published online: ((will be filled in by the editorial staff))

Reference

[1] Y. T. Chae, J. Kim, H. Park, and B. Shin, "Building energy performance evaluation of building integrated photovoltaic (BIPV) window with semi-transparent solar cells," *Applied Energy,* vol. 129, pp. 217-227, 2014.

[2] P. K. Ng, N. Mithraratne, and H. W. Kua, "Energy analysis of semi-transparent BIPV in Singapore buildings," *Energy and buildings,* vol. 66, pp. 274-281, 2013.

[3] M. Hiroshi, "RADIATION ENERGY TRANSDUCING DEVICE," Patent Appl. US3278811, 1961.

[4] A. Luque, A. Cuevas, and J. Ruiz, "Double-sided n+-p-n+ solar cell for bifacial concentration," *solar Cells,* vol. 2, no. 2, pp. 151-166, 1980.

[5] L. Janßen, H. Windgassen, D. L. Bätzner, B. Bitnar, and H. Neuhaus, "Silicon nitride passivated bifacial Cz-silicon solar cells," *Solar Energy Materials and Solar Cells,* vol. 93, no. 8, pp. 1435-1439, 2009, doi: 10.1016/j.solmat.2009.03.015.

[6] J. Liang, J. Yang, G. Zhang, and W. Sun, "Flexible fiber-type dye-sensitized solar cells based on highly ordered TiO2 nanotube arrays," *Electrochemistry Communications,* vol. 37, pp. 80-83, 2013.

[7] K.-M. Lee, W.-H. Chiu, V. Suryanarayanan, and C.-G. Wu, "Enhanced efficiency of bifacial and back-illuminated Ti foil based flexible dye-sensitized solar cells by decoration of mesoporous

SiO2 layer on TiO2 anode," *Journal of Power Sources,* vol. 232, pp. 1-6, 2013, doi: 10.1016/j.jpowsour.2012.12.094.

[8] C. Bu, Q. Tai, Y. Liu, S. Guo, and X. Zhao, "A transparent and stable polypyrrole counter electrode for dye-sensitized solar cell," *Journal of Power Sources,* vol. 221, pp. 78-83, 2013, doi: 10.1016/j.jpowsour.2012.07.117.

[9] X. Wu *et al.*, "13·9%-efficient CdTe polycrystalline thin-film solar cells with an infrared transmission of ~50%," *Progress in Photovoltaics: Research and Applications,* vol. 14, no. 6, pp. 471-483, 2006, doi: 10.1002/pip.664.

[10] A. Romeo, G. Khrypunov, S. Galassini, H. Zogg, and A. N. Tiwari, "Bifacial configurations for CdTe solar cells," *Solar Energy Materials and Solar Cells,* vol. 91, no. 15-16, pp. 1388-1391, 2007, doi: 10.1016/j.solmat.2007.03.010.

[11] S. Marsillac, V. Y. Parikh, and A. D. Compaan, "Ultra-thin bifacial CdTe solar cell," *Solar Energy Materials and Solar Cells,* vol. 91, no. 15-16, pp. 1398-1402, 2007, doi: 10.1016/j.solmat.2007.04.025.

[12] T. Nakada, "Microstructural and diffusion properties of CIGS thin film solar cells fabricated using transparent conducting oxide back contacts," *Thin Solid Films,* vol. 480-481, pp. 419-425, 2005, doi: 10.1016/j.tsf.2004.11.142.

[13] H. Deng *et al.*, "Novel symmetrical bifacial flexible CZTSSe thin film solar cells for indoor photovoltaic applications," *Nat Commun,* vol. 12, no. 1, p. 3107, May 25 2021, doi: 10.1038/s41467-021-23343-1.

[14] M. Espindola-Rodriguez *et al.*, "Bifacial Kesterite Solar Cells on FTO Substrates," *ACS Sustainable Chemistry & Engineering,* vol. 5, no. 12, pp. 11516-11524, 2017, doi: 10.1021/acssuschemeng.7b02797.

[15] Z. Song, C. Li, L. Chen, and Y. Yan, "Perovskite Solar Cells Go Bifacial-Mutual Benefits for Efficiency and Durability," *Adv Mater,* vol. 34, no. 4, p. e2106805, Jan 2022, doi: 10.1002/adma.202106805.

[16] S. H. Park *et al.*, "The application of camphorsulfonic acid doped polyaniline films prepared on TCO-free glass for counter electrode of bifacial dye-sensitized solar cells," *Journal of Photochemistry and Photobiology A: Chemistry,* vol. 245, pp. 1-8, 2012, doi: 10.1016/j.jphotochem.2012.07.002.

[17] Y.-F. Chiang, C.-H. Tsai, P. Chen, and T.-F. Guo, "Bifacial transparent solid-state dye-sensitized solar cell with sputtered indium-tin-oxide counter electrode," *Solar Energy,* vol. 86, no. 6, pp. 1967-1972, 2012, doi: 10.1016/j.solener.2012.03.004.

[18] Y.-S. Wang *et al.*, "Thickness-self-controlled synthesis of porous transparent polyaniline-reduced graphene oxide composites towards advanced bifacial dye-sensitized solar cells," *Journal of Power Sources,* vol. 260, pp. 326-337, 2014, doi: 10.1016/j.jpowsour.2014.02.090.

[19] W. Yang *et al.*, "Nitrogen plasma modified CVD grown graphene as counter electrodes for bifacial dye-sensitized solar cells," *Electrochimica Acta,* vol. 173, pp. 715-720, 2015, doi: 10.1016/j.electacta.2015.05.143.

[20] M. J. Shin *et al.*, "Semitransparent and bifacial ultrathin Cu(In,Ga)Se2 solar cells via a single-stage process and light-management strategy," *Nano Energy,* vol. 82, 2021, doi: 10.1016/j.nanoen.2020.105729.

[21] Y. Zhao *et al.*, "Regulating Energy Band Alignment via Alkaline Metal Fluoride Assisted Solution Post-Treatment Enabling Sb2(S,Se)3 Solar Cells with 10.7% Efficiency," *Advanced Energy Materials,* vol. 12, no. 1, 2021, doi: 10.1002/aenm.202103015.

[22] C. Qian *et al.*, "9.6%-Efficient all-inorganic Sb2(S,Se)3 solar cells with a MnS hole-transporting layer," *Journal of Materials Chemistry A,* vol. 10, no. 6, pp. 2835-2841, 2022, doi: 10.1039/d1ta09913b.

[23] K. K. Subedi *et al.*, "Nanocomposite (CuS) (ZnS)1 thin film back contact for CdTe solar cells: Toward a bifacial device," *Solar Energy Materials and Solar Cells,* vol. 186, pp. 227-235, 2018, doi: 10.1016/j.solmat.2018.06.025.

[24] K. K. Subedi *et al.*, "Enabling bifacial thin film devices by developing a back surface field using CuxAlOy," *Nano Energy,* vol. 83, 2021, doi: 10.1016/j.nanoen.2021.105827.

[25] S. S. Hegedus and W. N. Shafarman, "Thin-film solar cells: device measurements and analysis," *Progress in Photovoltaics: Research and Applications,* vol. 12, no. 23, pp. 155-176, 2004, doi: 10.1002/pip.518.

[26] X. Cui *et al.*, "Enhanced heterojunction interface quality to achieve 9.3% efficient Cd-free Cu2ZnSnS4 solar cells using atomic layer deposition ZnSnO buffer layer," *Chemistry of materials,* vol. 30, no. 21, pp. 7860-7871, 2018.

[27] P. Asogwa, "Effect of deposition medium on the optical and solid state properties of annealed MnO2 thin films," *J. Optoelectron Biomed. Mater,* vol. 2, pp. 109-17, 2010.

[28] K. O. Oyedotun *et al.*, "Some properties of manganese oxide (Mn-O) and lithium manganese oxide (Li-Mn-O) thin films prepared via metal organic chemical vapor deposition (MOCVD) technique," *Journal of Materials Science and Engineering B,* vol. 5, pp. 231-242, 2015.

[29] R. Naeem, M. A. Ehsan, R. Yahya, M. Sohail, H. Khaledi, and M. Mazhar, "Fabrication of pristine Mn 2 O 3 and Ag–Mn 2 O 3 composite thin films by AACVD for photoelectrochemical water splitting," *Dalton Transactions,* vol. 45, no. 38, pp. 14928-14939, 2016.

[30] B. Şahin, R. Aydin, and H. Cetin, "Tuning the morphological, structural, optical and dielectric properties of hausmannite (Mn3O4) films by doping heavy metal lead," *Superlattices and Microstructures,* vol. 143, p. 106546, 2020.

[31] J. Li *et al.*, "Defect-Resolved Effective Majority Carrier Mobility in Highly Anisotropic Antimony Chalcogenide Thin-Film Solar Cells," *Solar RRL,* vol. 5, no. 3, 2021, doi: 10.1002/solr.202000693.

[32] R. Tang *et al.*, "Hydrothermal deposition of antimony selenosulfide thin films enables solar cells with 10% efficiency," *Nature Energy,* vol. 5, no. 8, pp. 587-595, 2020, doi: 10.1038/s41560-020-0652-3.

[33] O. Madelung, *Semiconductors: data handbook*. Springer Science & Business Media, 2004.

[34] D. Pokhrel *et al.*, "Copper iodide nanoparticles as a hole transport layer to CdTe photovoltaics: 5.5 % efficient back-illuminated bifacial CdTe solar cells," *Solar Energy Materials and Solar Cells,* vol. 235, 2022, doi: 10.1016/j.solmat.2021.111451.

[35] D. P. Morgan and D. F. Kelley, "What Does the Transient Absorption Spectrum of CdSe Quantum Dots Measure?," *The Journal of Physical Chemistry C,* vol. 124, no. 15, pp. 8448-8455, 2020, doi: 10.1021/acs.jpcc.0c02566.

[36] A. Sharma, P. Kumar, B. Singh, S. R. Chaudhuri, and S. Ghosh, "Capacitance-voltage characteristics of organic Schottky diode with and without deep traps," *Applied Physics Letters,* vol. 99, no. 2, 2011, doi: 10.1063/1.3607955.

[37] J. Werner, A. F. Levi, R. T. Tung, M. Anzlowar, and M. Pinto, "Origin of the excess capacitance at intimate Schottky contacts," *Phys Rev Lett,* vol. 60, no. 1, pp. 53-56, Jan 4 1988, doi: 10.1103/PhysRevLett.60.53.

[38] Z. Fang *et al.*, "Perovskite-based tandem solar cells," *Science Bulletin,* vol. 66, no. 6, pp. 621-636, 2021.

[39] L. Wang *et al.*, "Ambient CdCl2 treatment on CdS buffer layer for improved performance of Sb2Se3 thin film photovoltaics," *Applied Physics Letters,* vol. 107, no. 14, 2015, doi: 10.1063/1.4932544.

WILEY-VCH

Table of Contents (ToC)

Bifacial and semitransparent $Sb_2(S,Se)_3$ solar cells for single-junction and tandem photovoltaic applications

Chen Qian, Kaiwen Sun, Jialin Cong, Huiling Cai, Jialiang Huang, Caixia Li, Rui Cao, Ziheng Liu, Martin Green, Bram Hoex*, Tao Chen*, Xiaojing Hao**

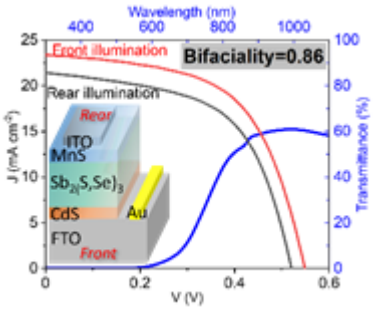

Bifacial and semitransparent $Sb_2(S,Se)_3$ solar cells exhibit exceptional bifaciality of 0.86 and satisfactory long-wavelength transmittance exceeding 60%, highly suitable for initial real-world applications that leverage their ability to effectively absorb tilted incident illumination and enhance performance by exploiting albedo. Furthermore, their compatibility with silicon solar cells enables their integration in tandem applications, unlocking further potential for promoted efficiency.